Soft Matter

Accepted Manuscript

This is an *Accepted Manuscript*, which has been through the Royal Society of Chemistry peer review process and has been accepted for publication.

Accepted Manuscripts are published online shortly after acceptance, before technical editing, formatting and proof reading. Using this free service, authors can make their results available to the community, in citable form, before we publish the edited article. We will replace this *Accepted Manuscript* with the edited and formatted *Advance Article* as soon as it is available.

You can find more information about *Accepted Manuscripts* in the Information for Authors.

Please note that technical editing may introduce minor changes to the text and/or graphics, which may alter content. The journal's standard Terms & Conditions and the Ethical guidelines still apply. In no event shall the Royal Society of Chemistry be held responsible for any errors or omissions in this *Accepted Manuscript* or any consequences arising from the use of any information it contains.

ROYAL SOCIETY OF CHEMISTRY

www.rsc.org/softmatter

Effects of Thermal Noise on the Transitional Dynamics of an Inextensible Elastic Filament in Stagnation Flow

Mingge Deng,[a] Leopold Grinberg,[b] Bruce Caswell [c] and George Em Karniadakis [a]*

[a] Division of Applied Mathematics, Brown University, Providence, RI 02912, USA
[b] T.J. Watson Research Center, IBM, Cambridge, MA 02142, USA
[c] School of Engineering, Brown University, Providence, RI 02912, USA

We investigate the dynamics of a single inextensible elastic filament subject to anisotropic friction in a viscous stagnation-point flow, by employing both a continuum model represented by Langevin type stochastic partial differential equations (SPDEs) and a Dissipative Particle Dynamics (DPD) method. Unlike previous works [1], the filament is free to rotate and the tension along the filament is determined by the local inextensible constraint. The kinematics of the filament is recorded and studied with normal modes analysis. The results show that the filament displays an instability induced by negative tension, which is analogous to Euler buckling of a beam. Symmetry breaking of normal modes dynamics and stretch-coil transitions are observed above the threshold of the buckling instability point. Furthermore, both temporal and spatial noise are amplified resulting from the interaction of thermal fluctuations and nonlinear filament dynamics. Specifically, the spatial noise is amplified with even normal modes being excited due to symmetry breaking, while the temporal noise is amplified with increasing time correlation length and variance.

1 Introduction

Bio-polymers, such as F-actin, protein fibers, DNA, and microtubules are all semiflexible elastic filaments. There are two unique characteristic properties distinguishing them from most of the other natural and synthetic polymers: they posess a certain stiffness that energetically suppresses bending, and they are to a high degree inextensible, i.e., their back-bone cannot be stretched or compressed too much. The cytoskeletons of cells and tissues are mostly built by such bio-polymers, thus, studying the dynamics of inextensible elastic filaments subject to hydrodynamic forces can be a first step towards understanding the cytoskeleton networks and tissue motions. Previous works focused mainly on the stretching dynamics of filaments with tension applied lengthwise [2–9], both with and without hydrodynamics. However, recent works on the dynamics of elastic filaments subject to hydrodynamic forces has revealed complex nonlinear dynamical behavior both in simple shear flows [10–15] and in the neighborhood of stagnation-point of stretching flows [6,16,17]. Specifically, the negative tension induced along the filament by simple hydrodynamic forces above some critical value can lead to buckling known as "stretch-coil" instability [16,18,19]. Hence, it is very important to fully understand the inextensible elastic filament dynamics for cell mechanics [20].

Suspended in stretching flow, these filaments respond as mesoscopic entities ($\sim \mu m$), and hence the forces on them, Brownian, hydrodynamic and elastic, are of the same order. This, in turn, implies the importance of thermal fluctuation so that the Brownian forces cannot be neglected. However, to the best of our knowledge, only a few papers have addressed the thermal fluctuation effects [10–12,21,22]. Moreover, nonlinear response due to the thermal noise has become a central topic in studies of various dynamical systems. For example, as was shown recently, thermal noise is greatly amplified in a dynamical system due to the interaction between stochasticity and nonlinearity near bifurcation points [23–27], i.e., low dimensional models with a small number of modes are sufficient to capture the physics in these complex systems only up to the bifurcation points, after which, higher modes will make significant contributions to the full dynamics.

The objective of the current work is to study the role of thermal fluctuations on the deformation of single linear filament subject to stretching and compression near a stagnation-point within a viscous flow. The filaments are represented by two models. The first is the inextensible elastic filament described as a continuous curve for which the solvent flow acts through the anisotropic viscous resistance and thermal noise, and the dynamics of the inextensible filament is governed by Langevin type stochastic partial differential equations (SPDEs) [12,28]. The second is a Dissipative Particle Dynamics (DPD) bead-spring chain model immersed in a solvent of DPD particles subject to the stagnation-point flow. Details about these two models are given in Sec. 2. These two models are then simulated by obtaining numerical solutions to the governing SPDEs and DPD equations, respectively (see Sec. 3). A reader who is not interested in technical details can skip directly to Sec. 4, where the main numerical results are obtained from each model. We use normal mode analysis to identify the stretch-coil transition and amplification of thermal noise during filament dynamics. These physical phenomena can also analyzed with Proper Orthogonal Decomposition (POD) analysis, which is included in the Appendix. Finally, a short conclusion about the limitation

of the current models and further work are included in Sec. 5.

2 Model Description

In this section, we present models for continuum inextensible elastic filaments and for bead-spring chains in stagnation-point flow.

2.1 Models of Linear Fibers

Most of the bio-polymers are generally modeled as inextensible elastic filaments whose deformations are dominated by elastic bending resistance. This contrasts with other long flexible molecules, which have little bending resistance, and are generally modelled as freely-jointed chains [11,13,14]. Two linear inextensible elastic filament models are simulated in our current work: a continuous elastic filament [29,30] and a bead-spring chain.

The energy functional for a *continuous* filament, constrained to be inextensible, is expressible as a line integral along its contour, $0 \le s \le L$, as follows:

$$E = \frac{1}{2}\int_{-L/2}^{L/2} ds\left(A(\kappa(s)-\kappa_0)^2 - \Lambda(s)\,(\partial_s \mathbf{r})^2\right), \qquad (1)$$

where θ and $\kappa = \partial_s\theta(s)$ are the tangent angle and the curvature at arc length s as shown in Figure 1(upper), respectively, and κ_0 is zero for a rigid rod filament. Bending resistance is characterized by the flexural rigidity, which in the theory of elastic beams is given by $A = GI$, with a material modulus G and second moment of cross-section area I [31]. By definition a filament is very thin, and filament theory is applied to entities where the cross-section dimensions are not easily determined. Thus, A is the preferred elastic parameter to characterize the bending elasticity. The second term of the integrand introduces the Lagrange multiplier $\Lambda(s)$ to impose the local constraint of inextensibility by the requirement that the tangent vector $\partial_s\mathbf{r}$ be of constant magnitude along the entire filament contour length. Division of Eq.(1) by k_BT and with all lengths scaled by L yield the dimensionless total filament elastic energy E/k_BT relative to the energy imposed on it by the thermal fluctuations. Within the integral, the dimensionless coefficient of the local elastic term becomes $\beta = A/(k_BTL)$, a measure of the local bending moment $\mathbf{M}(\mathbf{s}) = \mathbf{A}(\kappa(\mathbf{s}) - \kappa_\mathbf{0})$ relative to the moment imposed by the thermal transverse load. At the mesoscopic dimensions, where thermal fluctuations are important, an alternative measure of bending resistance is the persistence length l_P related to β by

$$\beta = \frac{A}{k_BTL} = \frac{l_p(d-1)}{2L}, \qquad (2)$$

where d is the dimension of the deformation space. A Langevin type equation models the motion of an elastic inextensible filament immersed in a continuous Newtonian solvent. The neutrally buoyant filament, of radius $a \sim \mathbf{O}(\mu m)$, $a/L \ll 1$, experiences hydrodynamic resistance governed by the Stokes equation, which exceeds inertia by several orders of magnitude; hence, inertial forces can be safely neglected. Also, the disturbance of the flow field by the filament motion is absorbed into the Brownian force effects. Thus, the mesoscopic level equation of motion reduces to a balance between three forces: the Brownian force ($\sim k_BT/L$), the hydrodynamic force ($\sim \mu\dot{\varepsilon}L^2$) and the elastic bending force ($\sim A/L^2$). The motion generated by these forces must satisfy the local inextensibility of the filament, which requires the magnitude of its tangent vector to be constrained locally to be $|d\mathbf{r}/ds| = 1$ along its contour; the latter condition yields the line tension generated by the Lagrange multiplier. Finally, the governing equation is written as the sum of the deterministic forces balanced by the fluctuating stochastic driving force:

$$\eta\mathbf{D}[\partial_t\mathbf{r} - \mathbf{u}(\mathbf{r})] + \left(A\frac{\partial^4\mathbf{r}}{\partial s^4} + \partial_s\big(\Lambda(s)\partial_s\mathbf{r}\big)\right) = \mathbf{f}_{stoch}(s,t), \quad (3)$$

where $\mathbf{D}$ is the dimensionless anisotropic drag tensor, $\mathbf{D} = \mathbf{I} - \frac{1}{2}\partial_s\mathbf{r}\otimes\partial_s\mathbf{r}$, and $\eta = (2\pi)\mu/ln(L/a)$ is the effective viscosity derived from the known Stokes resistance for a rigid rod of radius a. The latter is usually approximated by rough estimates, but the inaccuracy is tolerable since it appears only in the logarithm. This form of the hydrodynamic resistance is accurate provided the filament remains nearly straight, but as it departs from a linear configuration accuracy is lost. Also, the configuration of a compliant filament may depart so far from straightness as to induce significant hydrodynamic interactions between its parts. These restrictions are avoided for the DPD model since the DPD solvent accounts implicitly for hydrodynamic effects. The tensor Lagrange multiplier $\Lambda(s)$ is an unknown introduced to impose the inextensibility constraint, and is the one-dimensional analog of the pressure Lagrange-multiplier employed to impose incompressibility on a continuum velocity field. The Langevin equation is scaled with the contour length L, the hydrodynamic time $\dot{\varepsilon}^{-1}$ and the characteristic Brownian force k_BT/L to yield the dimensionless equation,

$$\partial_t\mathbf{r} - \Gamma\cdot\mathbf{r} = \frac{\mathbf{D}^{-1}}{\alpha}\left(-\beta\frac{\partial^4\mathbf{r}}{\partial s^4} - \partial_s\left(\Lambda(s)\partial_s\mathbf{r}\right) + \mathbf{f}_{stoch}(s,t)\right), \quad (4)$$

where Γ is the velocity gradient tensor given below. Hence, the solution of this equation requires, in addition to β, the Peclet number [32] α defined as

$$\alpha = \frac{\eta\dot{\varepsilon}L^3}{k_BT}, \qquad (5)$$

which measures the hydrodynamic forces induced by the stretching flow relative to the thermal Brownian force. The dimensionless parameter β measures the elastic bending force relative to the thermal Brownian force, which is the typical definition of relative persistence length in polymer science [28]. The ratio $\alpha/\beta = \eta\dot{\varepsilon}L^4/A$ measures the relative strengths of the viscous and elastic forces. Its limiting values ($\to 0$, $\to \infty$), respectively, indicate a nearly-rigid rod dominated by bending

elasticity and a flexible string drawn out to align symmetrically by the dominant hydrodynamic forces about the stagnation point. However, the latter configuration ignores the effects of the Brownian fluctuations which induce a coiled configuration, as will be seen below. The key parameter α/β in our manuscript is essentially the same as η in Guglielmini et al.[1], μ in Manikantan et al.[33] and Σ in Kantsler et al.[16], but with different constant pre-factors. In the limit of vanishing hydrodynamic force ($\alpha \to 0$), the Langevin equation reduces to a linear problem, i.e, elastic bending vibrations forced by Brownian fluctuations. The Brownian force $\mathbf{f}_{stoch}(s,t)$ satisfies the fluctuation-dissipation theorem as follows:

$$\begin{aligned} \langle \mathbf{f}_{stoch}(s,t) \rangle &= \mathbf{0} \\ \langle \mathbf{f}_{stoch}(s,t) \otimes \mathbf{f}_{stoch}(s',t') \rangle &= 2\alpha \mathbf{D} \delta(s-s') \delta(t-t') \end{aligned} \tag{6}$$

Therefore, $\mathbf{f}_{stoch}$ represents white-noise excitation and can thus be expressed in terms of generalized derivatives of the multi-dimensional standard Wiener process,

$$\mathbf{f}_{stoch} = \sqrt{2\alpha}\mathbf{C}\frac{\partial^2 \mathbf{W}(s,t)}{\partial s \partial t}. \tag{7}$$

Here, $\mathbf{C}$ is a matrix satisfying $\mathbf{C}\mathbf{C}^T = \mathbf{D}$ and according to[25], $\mathbf{C} = \mathbf{I} + (\frac{\sqrt{2}}{2} - 1)\partial_s \mathbf{r} \otimes \partial_s \mathbf{r}$.

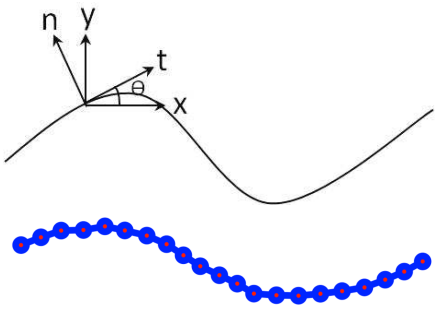

Fig. 1 Sketches of (upper) continuous filament with geometric parameter definitions and (lower) bead-spring chain model.

The bead-spring chain model used in the *particle-based* simulations, as shown in Figure 1(lower), is designed to mimic the continuous filament. The discrete elastic energy E_{bs} is a sum of angle-dependent bending energies and stretching energies for every consecutive pair of bonds,

$$E_{bs} = \sum \frac{1}{2} k_a (\theta - \theta_0)^2 + \sum \frac{1}{2} k_s (b - b_0)^2, \tag{8}$$

where k_a and k_s are the elastic constants for bending and stretching, respectively. The deformation measures between consecutive bonds $\theta - \theta_0$ and $b - b_0$, for bending and stretching respectively, are taken relative to their equilibrium reference values θ_0, b_0. In this work, θ_0 is taken to be π along the entire contour, which sets the reference state to be a straight rod with b_0 determined by the number of bonds. The constraint of inextensibility is approximated locally with very stiff connectors (large k_s) between every pair of consecutive beads. Another equation incorporates the bending constant k_a into the persistence length l_P analogously to equation (2) of the continuous filament case as

$$l_P = \frac{k_a b_0}{k_B T}. \tag{9}$$

Comparison of the two definitions of the persistence lengths, equations (2) and (9), suggests that the filament and the bead-spring chain models are elastically equivalent provided $k_a b_0 = 2A/(d-1)$. In addition, the bond spring constant k_s needs to be large enough to approximate the local constraints of inextensibility. This in turn limits the simulation time steps to very small value.

2.2 Stagnation-Point Flow

The stagnation-point flow has long been realized in the four-role-mill apparatus of Lagnado et al. and Yang et al., respectively[34,35], and has been employed in the study of drops and other objects of macroscopic dimensions[36]. The stagnation-point flow can be realized in the cross micro-channel arrangement of Kantsler & Goldstein[16] to observe the response of mesoscopic particles such as actin molecules in the vicinity of the stagnation point. The micro-channel system requires smaller sample volumes, and hence appears to be more suitable for the observation of macromolecules, cells, etc.. In the vicinity of the stagnation point the velocity field $\mathbf{v}(\mathbf{r})$ is spatially homogeneous, and can be written as,

$$\mathbf{v}(\mathbf{r}) = \Gamma \cdot \mathbf{r}\,, \quad \Gamma = \dot{\varepsilon} \begin{bmatrix} 0 & 1 \\ -1 & 0 \end{bmatrix}, V = \dot{\varepsilon}\sqrt{(x^2+y^2)}\,, \tag{10}$$

with V the velocity magnitude, $\dot{\varepsilon}$ the shear rate and Γ the velocity field matrix. For particle-based simulation methods such as DPD, simple flows (i.e., shear flows) are commonly generated by imposing a constant driving force (Poiseuille flow), equivalent to a pressure gradient, or a driving velocity on the boundary shear planes (Couette flow). However, with a particle based method it is not trivial to implement the stagnation-point flow together with periodic boundary conditions. Recently, Pan et al.[37] devised a periodic uniaxial stretching flow for DPD simulations in which a smaller box is placed inside an outer larger box. Periodic boundary conditions are applied on the surfaces of the latter, while the flow is driven by a distribution of velocities on opposing vertical surfaces of the inner box. By reversal of the direction of the driving velocities stretching/compressing can be imposed along the x/y-axes. Known analytic stretching flows are defined on infinite domains, and hence the box-inside-a-box is a convenient way to have fully periodic conditions with simplicity of implementation. However, the outer box size should be large enough to ensure minimal effect on the stagnation-point flow. Our experience is that the large size and slow convergence to the steady state makes

the box-in-a-box scheme computationally expensive. Furthermore, the stagnation stretch rate cannot be specified, and has to be determined by trial. We have developed a driving-force field to yield a stagnation-point flow in a DPD computational box with periodic boundary conditions. The new scheme takes advantage of the well-known fact that the Navier-Stokes equation is satisfied by a potential flow. The $x-y$ plane of the box is a periodic square in a lattice of vortices. It is bounded by streamlines, and contains four counter-rotating vortices located at the centers of each quadrant. In potential flow, Bernoulli's equation is $H = 1/2\rho\mathbf{v}^2 + P + \rho\chi =$ constant. The velocity field can be thought of as being driven by the body force per unit mass $\nabla(\chi + P/\rho)$, which by Bernoulli's equation is $\nabla\mathbf{v}^2$. The derivation of this driving force will be given in a forthcoming publication, where it will be shown that use of this driving force yields accurate simulations. Furthermore, excellent economy is achieved due to rapid convergence from a startup at rest to the steady state. The simulated streamline and pressure pattern is shown in Figure 2 (left), and the velocity-vector pattern in the vicinity of the center shows it to be a stagnation point; see the velocities along the centerlines $x = 0, y = 0$ plotted in Figure 2(right). In the DPD simulation, a single bead-spring filament model is released with its center of mass at the stagnation-point (center of simulation box) of the flow shown in Figure 2(left). No constraints are imposed on the motion of fiber near stagnation-point, while Guglielmini et al.[1] use Brownian dynamics to study an elastic filament tethered to the stagnation point. The kinematics of fiber is then recorded as functions of time, as shown in Figure 3 as well as online video. Because of the accurate symmetry of the analytic stagnation-point flow driving the filament motion, the dwell time of the filament in the region of uniform strain rate was always sufficient to observe its complete reorientation along the stretching axis.

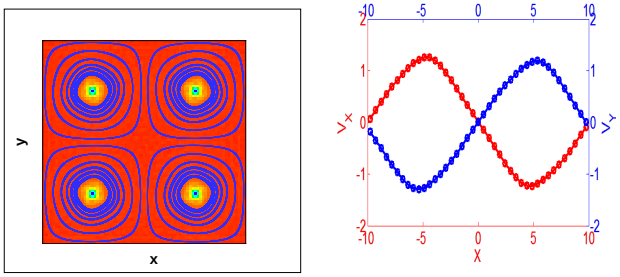

Fig. 2 (left) Streamlines derived from DPD simulations of a Newtonian fluid undergoing stagnation-point flow in the periodic box; (right) Velocities along the X(red)- and the Y(blue)-axis. The strain rate is uniform (linear velocities) for $X, Y < +/-4$.

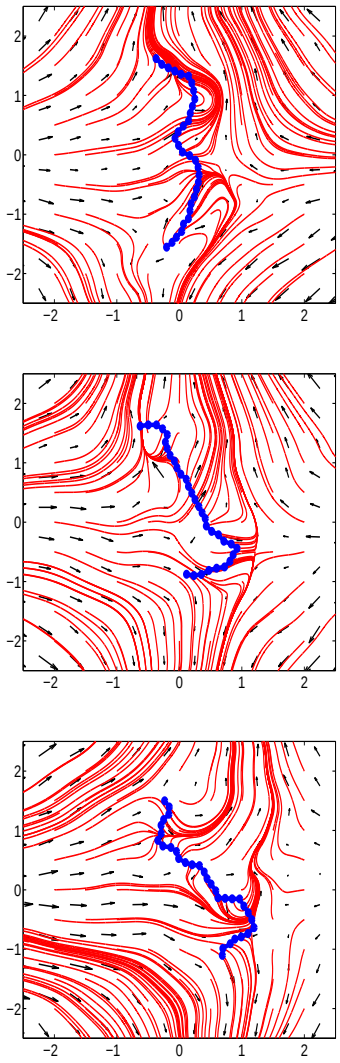

Fig. 3 Instantaneous streamlines and velocity vectors showing the disturbance of the stagnation-point flow caused by the bead-spring chain constrained to deform in the plane. (see online video)

3 Numerical Methods

With sufficient depth, the Yang et al.'s four-role-mill apparatus should allow a suspended object to move freely in any direction, and therefore it is appropriate to simulate the resulting disturbance flow as fully three-dimensional. However, in the crossed-channel configuration, the classical stagnation-point flow is realized only in the mid-vertical plane, and the small gap will tend to constrain a suspended object to move within that plane. This is the motivation for the 2D simulations described below.

3.1 Numerical Methods for Governing SPDEs

The numerical approach taken here was inspired by Chorin's method for incompressible Navier-Stokes equation[38]. First, we introduce the auxiliary systems for the position $\mathbf{r}(\mathbf{s},\mathbf{t})$ along the

fiber, as follows

$$\begin{aligned}
&\partial_t \mathbf{r} - \Gamma\cdot\mathbf{r} = \frac{\mathbf{D}^{-1}}{\alpha}\left(-\beta\frac{\partial^4\mathbf{r}}{\partial s^4} - \partial_s\left(\Lambda(s)\partial_s\mathbf{r}\right) + \mathbf{f}_{stoch}(s,t)\right)\\
&\frac{\partial(\delta\Lambda)}{\partial t} + \left(\frac{\partial\mathbf{r}}{\partial s}\right)^2 - 1 = 0\\
&\Lambda(s=0) = \Lambda(s=1) = 0\\
&\frac{\partial^2\mathbf{r}}{\partial s^2}(s=0,s=1) = \frac{\partial^3\mathbf{r}}{\partial s^3}(s=0,s=1) = 0
\end{aligned} \tag{11}$$

We shall call δ the artificial extensibility, and t in the second equation is an auxiliary variable whose role is analogous to that of time in extensible fiber problem. Numerically, we choose $\delta \sim \mathbf{O}(\Delta t)$, and our auxiliary system indeed converges to inextensible filament system as Δt goes to zero.

The auxiliary system (11) can be used with various difference schemes. Here, considering the stiffness introduced by the elastic term $\frac{\partial^4\mathbf{r}}{\partial s^4}$, the SPDEs are discretized discretized by central finite difference in space and a stiffly-stable scheme in time. To this end, we consider $Nt+1$ discrete points in time $t^i = i\Delta t$ with $i \in \{0,1,2,...,Nt\}$, and the arc length in space is discretized uniformly by $Ns+1$ nodes $s_k = k\Delta s$, $k \in 0,1,2,...,Ns$ and $\Delta s = 1/Ns$. A staggered grid is used to calculate $\mathbf{r}$ and Λ for stability reasons, i.e., the displacements $\mathbf{r}$ are calculated at the center points of each interval with total Ns points, while the line tensions are updated every timestep on the boundaries of each interval with total $Ns+1$ points. Ghost points are used to approximate the high-order derivatives near the boundaries. We approximate the stochastic force as piece-wise constant on distinct time and space intervals, Δs and Δt, i.e., the discrete stochastic forces are Gaussian random numbers and are uniquely characterized by zero mean value and the covariance matrix:

$$\mathbf{f}^i_{stoch\,k} \approx \sqrt{\frac{2\alpha}{\triangle t\triangle s}}\mathbf{C}^i_k\mathscr{N}(0,1) \tag{12}$$

with $\mathscr{N}(0,1)$ denoting the normalized Gaussian distribution. Finally, the discretized equations can be written using a third-order stiffly stable scheme[39] as

$$\begin{aligned}
\mathbf{r}_k^{i+1} &= \frac{18}{11}\mathbf{r}_k^i - \frac{9}{11}\mathbf{r}_k^{i-1} + \frac{2}{11}\mathbf{r}_k^{i-2} + \frac{6}{11}\Delta t\left(\mathbf{F}_k^{i+1} + \mathbf{f}^{i+1}_{stoch\,k}\right)\\
\Lambda_k^{i+1} &= \frac{18}{11}\Lambda_k^i - \frac{9}{11}\Lambda_k^{i-1} + \frac{2}{11}\Lambda_k^{i-2} + \frac{6}{11}\frac{\Delta t}{\delta}G_k^{i+1}
\end{aligned} \tag{13}$$

where $\mathbf{F}$ and G are numerical discretizations of the terms $\Gamma\cdot\mathbf{r} + \frac{\mathbf{D}^{-1}}{\alpha}\left(-\beta\frac{\partial^4\mathbf{r}}{\partial s^4} - \partial_s\left(\Lambda(s)\partial_s\mathbf{r}\right)\right)$ and $\left(1-(\partial_s\mathbf{r})^2\right)$, respectively, with central differences. At each time step, these coupled two equations are iteratively solved by fixed-point iteration. In equation (13), the stochastic terms are treated in the Ito sense. We then sample the stochastic trajactories with the Monte Carlo method. High order discretization formulas are used both in time and space, nevertheless, we can only achieve first-order convergence in the weak sence because of the Wiener process, as shown in Figure 4.

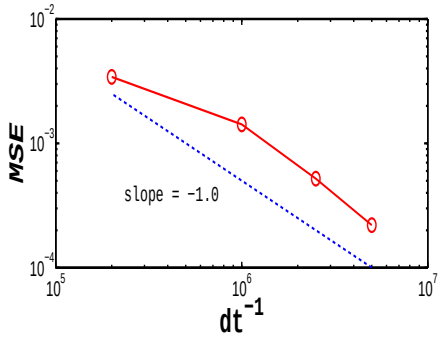

Fig. 4 Numerical (weak) convergence of the solution of equation (4) as measured by the mean square error (MSE) of filament end-to-end distance as a function of time step Δt. The exact solutions are computed with $\Delta t = 10^{-9}$.

3.2 Dissipative Particle Dynamics Simulation

We then study the inextensible fiber dynamics subject to stagnation-point flow by employing DPD simulations. DPD is a mesoscale method for studying coarse-grained models of soft matter and complex fluid systems over relatively long length and time scales, see[40–42]. In DPD, the particles interact via pairwise additive forces, consisting (in the basic form) of three components: (i) a conservative force $\mathbf{f}^C$; (ii) a dissipative force, $\mathbf{f}^D$; and (iii) a random force, $\mathbf{f}^R$. Hence, the total force on particle i is given by $\mathbf{f}_i = \sum_{i\neq j}\left(\mathbf{f}^C_{ij} + \mathbf{f}^D_{ij} + \mathbf{f}^R_{ij}\right)$, where the sum acts over all particles within a cut-off radius r_c. Specifically, in our simulations we have

$$\mathbf{f}_i = \sum_{i\neq j} a_{ij}\omega(r_{ij})\hat{\mathbf{r}}_{ij} - \gamma\omega^2(r_{ij})(\hat{\mathbf{r}}_{ij}\cdot\hat{\mathbf{v}}_{ij})\hat{\mathbf{r}}_{ij} + \sigma\omega(r_{ij})\frac{\zeta_{ij}}{\sqrt{\triangle t}}\hat{\mathbf{r}}_{ij} \tag{14}$$

where a_{ij} is a maximum repulsion between particles i and j. We set $a_{ij} = a = 25.0$ for both solvent and filaments particles in our simulations. r_{ij} is the distance with the corresponding unit vector $\hat{\mathbf{r}}_{ij}$, $\hat{\mathbf{v}}_{ij}$ is the difference between the two velocities, ζ_{ij} is a Gaussian random number with zero mean and unit variance, and γ and σ are parameters coupled by $\sigma^2 = 2\gamma k_B T$[43]. Typically, the weighting functions $\omega(r_{ij})$ are given by

$$\omega(r_{ij}) = \begin{cases} 1 - \frac{r_{ij}}{r_c} & r_{ij} < r_c \\ 0 & r_{ij} \geq r_c. \end{cases} \tag{15}$$

The filaments are represented as bead-spring chains with $N = 32$ segments, with additional bond and angle forces $(-\nabla E_{bs})$ derived from equation (8). The average particle number density of the DPD solvent is $\rho = 3.0r_c^{-3}$ and the temperature is set at $k_BT = 1.0$. The simulations are performed using a modified version of the DPD code based on the open source code LAMMPS, see[44]. Time integration of the equation of motion is obtained by a modified velocity-Verlert algorithm, first proposed by[41], with time step $\Delta t = 0.001$ (in DPD time units).

4 Results and Discussion

In order to obtain a quantitative understanding of the dynamics of a fiber undergoing large distortions near the stagnation-point of flow, we interpret the solutions of system (Eq.(11)) in terms of the shape angle θ. Previous studies[16] have employed the eigen-modes analysis of the familar transverse displacement of elastic beam theory. However, such displacements become increasingly difficult to interpret for fiber distorted far beyond straight. Thus, normal modes analysis[45] of angle θ is used to study the fiber deformation during its motion. The bending moment $\mathbf{M}$ due to the transverse load along the fiber is $A(\kappa(s)-\kappa_0)$, and the differential of the elastic energy at an arbitrary point s along the fiber is $dE = A(\kappa(s)-\kappa_0)^2 ds$. Hence, the shape angle can be expressed as $\theta = \int(1/MdE)$. For a nearly straight fiber aligned with the stretching flow the bending load will be mainly that imposed by the thermal fluctuations. Thus, $\mathbf{M}$ will be $\mathscr{O}(k_BT)$ while dE is $\mathscr{O}(A/L)$, and hence $\theta \sim \mathscr{O}(\beta)$. However, as the fiber becomes highly distorted the hydrodynamic drag will also contribute to $\mathbf{M}$, and we then must include α in the functional denpendence of θ.

4.1 Normal Modes Analysis

We can express the shape $\theta(s)$, as defined in Figure 1, as a superposition of normal "modes",

$$\theta(s,t) = \sum_{q=0}^{\infty} u_q(t)\phi_q(s) \tag{16}$$

where u_q and ϕ_q are, respectively, the temporal and spatial normal modes, where $\phi_q(s)$ are complete set of orthogonal basis functions. The choice of the eigen-functions of the biharmonic operator with natural boundary conditions ($\partial_s\theta(-L/2) = \partial_s\theta(L/2) = 0, \partial_{ss}\theta(-L/2) = \partial_{ss}\theta(L/2) = 0$) as appropriate normal modes is motivated by the term with this highest spatial derivative in the equation of motion. Kantsler et al.[16] represented the displacements in terms of normal modes derived from the full elastic-beam equation in the limit of small displacements. It is not clear if such modes are appropriate for large distortions. An alternative set of modes is numerically derived in the Appendix by a Proper Orthogonal Decompostion(POD). Thus, the normal modes are determined by

$$\phi_{ssss} - \Lambda_q\phi = 0\ ,\ \ \Lambda_q = k_q/(\pi AL)^4\ , \tag{17}$$

where k_q is the q-th root of $\frac{1}{2}\cos(x)(e^x+e^{-x})-1=0$ and the eigenfunctions ϕ_q of this biharmonic operator are of the form,

$$\phi_q(s) = A\sin k_q s + B\sinh k_q s + D\cos k_q s + E\cosh k_q s \tag{18}$$

The coefficients are determined by the boundary conditions, and the first five normal modes are shown in Figure 4.

Here, we note that the eigen-functions of the full operator $\beta\frac{\partial^4\mathbf{r}}{\partial s^4} + \partial_s((\Lambda(s))\partial_s\mathbf{r})$, which correspond to the eigen-modes of fiber dynamics, cannot be obtained analytically since the tension $\Lambda(s)$ is unknown in general. For a nearly straight fiber aligned along the stretching or compression axis with small distortions, the tension $\Lambda(s)$ can be obtained analytically. In such case, the eigen-functions for the displacement are also obtained analytically by Kantsler et al.[16]. However, here, we study the fiber deformation during an entire cycle of fiber rotating from aligned along compression axis to stretching axis. The eigen-modes for angle θ instead of displacement are simply chosen as the eigen-functions of the biharmonic operator with natural boundary conditions. We only include the linear part of the deterministic operator, thus, these eigen-modes shown here do not correspond to real dynamic modes. We projected the full modes onto these linear normal modes for both geometric and computational reasons, and these linear normal modes are appropriate to study fiber deformations, because they form a complete set. Moreover, the tension $\Lambda(s)$ along the fiber changes sign from negative to positive during a full rotation, and hence the nonlinear term contribution cancels out (though not perfectly to zero) in an average sense. This is one of the main reasons that we chose the linear eigen-modes in addition to simplifying the computation. The real dynamic modes can be obtained numerically via Proper Orthogonal Decomposition (POD) over a certain time window, i.e., before significant buckling and reorientation, the POD modes correspond to the analytical eigen-modes obtained by Kantsler et al.[16]. A simple comparison between POD and normal modes is included in the Appendix. The spatial normal modes of Eq.(17) shown in Fig. 4 are appropiate to describe the deformed fiber by means of the shape angle θ for all levels of distortion. The linearity of the operator of Eq.(17) guarantees that the spatial modes will remain unchanged for all levels of non-linearity. For a simple scenario, if there are no interactions or correlations between each mode dynamics, i.e., the mode dynamics is all decoupled, the bending energy can be represented as quadratic summation

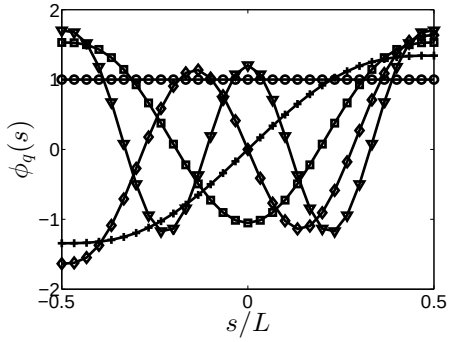

Fig. 5 First five normal modes (eigenfunctions) for the biharmonic operator with boundary conditions (Eq.18), cycle, cross, rectangle, diamond and triangle symobls represent 0th, 1st, 2nd, 3rd and 4th mode, respectively.

of the normal modes amplitudes, i.e. $U = \frac{1}{2}A\sum_{q=1}^{\infty} k_q^2 u_q^2$. Then, each quadratic term contributes an $1/2k_BT$ from the equipartition theorem, thus, we have $u_q^2 = \frac{k_BT}{A}\frac{1}{k_q^2}$. However, it is not true for inextensible filament dynamics here due to the nonlinear interactions between different modes, which arise from the local inextensible constraint.

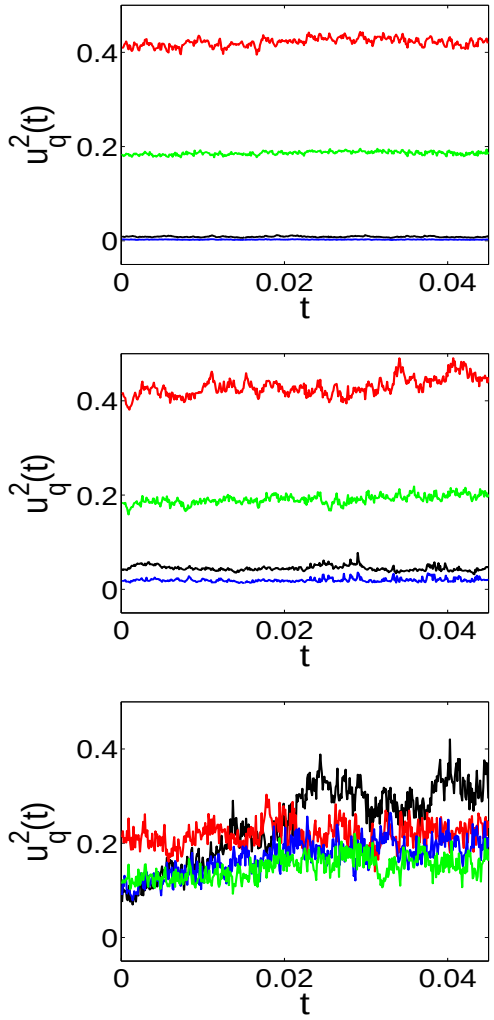

Fig. 6 First four normal modal energies as functions of dimensionless time at (a) $\alpha/\beta = 1.0$, (b) $\alpha/\beta = 10.0$, (c) $\alpha/\beta = 100.0$. Even and odd modes are represented as: by red and green 2nd and 4th, black and blue the 1st and 3rd, respectively. All of the data is derived from normal mode analysis of the numerical solution of equation (4).

4.2 Numerical Results

First, we show that the spatial modes of the filament motion can be seperated into symmetric (even) and antisymmetric (odd) relative to the mass center depending on whether under the transformation $\mathbf{r} - > -\mathbf{r}$ they are even or odd functions. Our results show that for $\alpha/\beta \leq 1$ odd modes are suppressed, which indicates fore-aft symmetry (Figure (6a)). As we increase α/β, the first mode is excited (Figure (6b)), further, for $\alpha/\beta \gg 1$, odd modes are excited, which implies that symmetry is broken as in Figure (6c). The even/odd modes behaviour is mainly because of the anti-symmetry of the eigen-functions of the linear biharmonic operator with natural boundary conditions. The eigen-functions in Eq.(18) only keep the first and last two terms for even and odd modes, respectively. Essentially, these phenomena come from the geometric constraints. Since our decomposition is done on the angle, the 0th mode corresponds to the pure rotation, which has the most dominant energy.

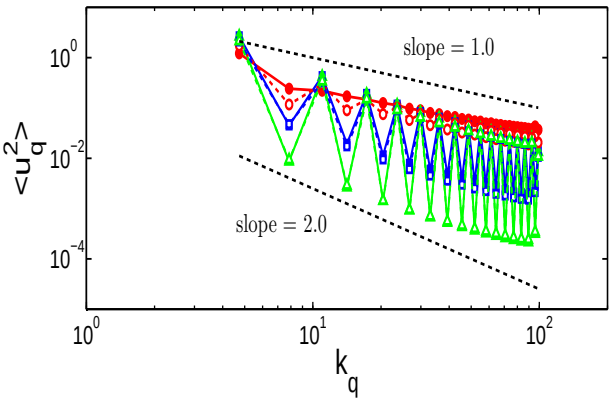

Fig. 7 Time average normal modes energy as functions of mode number k_q, with $\alpha/\beta = 100.0$ (red), 10.0 (blue), 1.0 (green). Data represented by solid symobls are derived from the numerical solution of continuum SPDEs, while data represented by open symbols are obtained from DPD simulations.The upper and lower dashed lines are reference lines for linear and quadratic decay, respectively.

An alternative way to illustrate the amplitude data is displayed in Figure 7, where the time averaged values of u_q^2 are plotted against mode number k_q display a sawtooth-trend due to the suppression of odd modes (two to three orders smaller than the even modes) and follow the equi-partition theorem for small $\alpha/\beta \leq 1$, i.e., the modal energy exhibits k_q^{-2} decay, as indicated by the dashed line with $slope = 2.0$. However, the modal energy decay is much slower for large $\alpha/\beta \gg 1$, which is indicated by a dashed line with $slope = 1.0$, and the sawtooth behavior disappears due to the excitation of odd modes (compared to even modes).

To further investigate the modal dynamics in time, we show the probability distribution functions (PDFs) of δu_q defined as

$$\delta u_q(t) = u_q(t) - \langle u_q(t) \rangle \tag{19}$$

in Figure 8, compared to a normal distribution fitting. The corresponding variances increase continuously as we increase $\frac{1}{\alpha/\beta}$, see inset in Figure 9. There is a three orders increase of variance within our parameters range, which implies that a

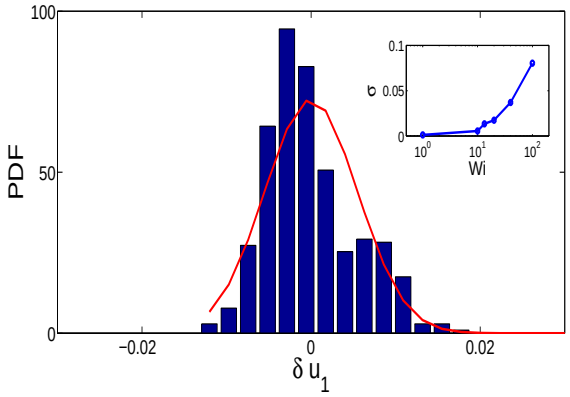

Fig. 8 PDF of δu_1 with $\alpha/\beta = 10.0$. (inset) PDF variance of δu_1 as a function of α/β.

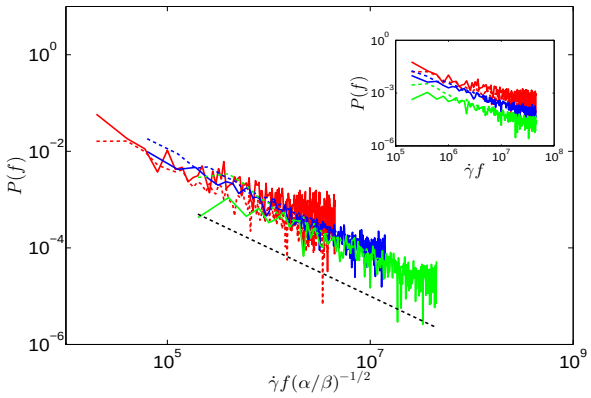

Fig. 9 Power spectral density function as a function of dimensionless frequency scaled with $\dot{\varepsilon} f/(\alpha/\beta)^{1/2}$ and (inset) original data, (from top to bottom)red, blue and green lines represent $\alpha/\beta = 100.0$, $\alpha/\beta = 10.0$ and $\alpha/\beta = 1.0$, respectively, with $\alpha = 10.0$. Data of solid and dashed lines are from solution of SPDEs and DPD simulations, respectively.

significant amplification of thermal fluctuations is taking place. Another interesting physical property for studying modal dynamics is the autocorrelation function, which is defined in the usual way as,

$$C_q(t) = \left\langle \delta u_q(t_0+t)\, \delta u_q(t_0) \right\rangle . \tag{20}$$

A useful observable to get insight into the stochastic behavior in time is the power spectral density (PSD) $P(f)$, which is the Fourier transform of the autocorrelation function $C_q(t)$, i.e., $P(f) := \mathrm{FFT} C_q(t)$. In Figure 9, we show the PSD of the first mode u_1, at several values of α/β. For large frequencies (short time regime), the PSDs obey the same power law $P(f) \propto (\dot{\varepsilon} f)^{-1}$. We note that our results are from 2D simulation, thus the slopes here are different from previous 3D studies[12]. All of these PSD data with different parameters collapse onto a single line with a simple rescaling $f \sim f/(\alpha/\beta)^{1/2}$. However, at small frequencies (long time regime), there is a pronounced increase in PSD with larger α/β, indicating stronger long-time correlations due to the interaction between nonlinearity and stochasticity.

To further quantify the Euler-buckling like instability and the transition point, we define k^* motivated by a similar expression derived empirically as a wrinkling criterion for vesicle membranes in previous studies[23,24]

$$k^* = \sqrt{\sum_{q=2}^{12} q^2 |u_q|^2 / \sum_{q=2}^{12} |u_q|^2} \tag{21}$$

The results both from the continuous filament model and the bead-spring chain model show that a transition occurs with α/β increasing to $\mathcal{O}(1)$ as in Figure 10. This interesting transition can also be identified by the average end-to-end distance R_f of the fiber as shown in Figure 11. This is the Euler-buckling like transition observed in previous experimental studies[16]. The departure in the flexible limit $\alpha/\beta \to \infty$ appears to be due to the use of steady flow Stokes resistence in continuous filament model Eq.(3), which is valid only for rigid rods. In the coil regime, the hydrodynamic resistance is underestimated in the continuum model. Thus, the results from the continuum model will be closer to the DPD results if we increase the hydrodynamic resistance coefficient η to 2η, while keeping α/β the same. These results and sensitivities are shown in Figures 10 and 11. Another difference between the two models originate from the hydrodynamics near the filament and the disturbance to the steady flow field by the filament deforming dynamics. The DPD model captures the instantaneous hydrodynamic interactions of the fluctuating flow field shown in Figure 3, and a more detailed video included as supplementary material.

Throughout the paper, α/β is used to measure the system, which is also adopted by other deterministic models[16], i.e., models that do not include thermal fluctuations. However, a short discussion about these dimensionless parameters is needed for stochastic models, when the thermal energy dominates. We note that $\alpha = \dot{\varepsilon}\tau$ has the form of a Weissenberg number, with $\tau = \frac{\eta L^3}{k_B T}$ corresponding to the time the center of mass of the fiber takes to diffuse its own contour length, which is independent of the persistence length l_P. Thus, it seems more appropriate to consider the fiber relaxation time as the characteristic time, since we focus on fiber deformation dynamics. The characteristic relaxation time is widely used to study flexible polymer extension with hydrodynamic effects. For weak bending resistance, we can renormalize the semiflexible fiber into freely-jointed chain model with effective Kuhn length l_P and number of segments L/l_P. Motivated by the Zimm model for flexible polymers[46], we then define the relaxation time to

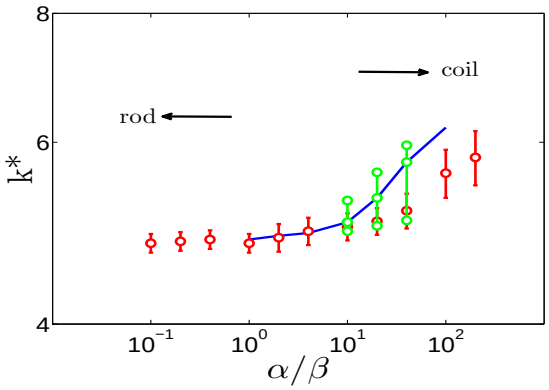

Fig. 10 Critical mode number k^* for buckling instability as a function of α/β determined from the planar motion of the Langevin filament and the 2D motion of the DPD bead-spring chain with $\alpha = 10.0$. Data for the solid blue line and open red symbols are from numerical solution of SPDEs and DPD simulations, respectively. The green symbols represent the variation of k^* as the hydrodynamic resistance coefficients in the continuum models are changed from η to 2η (lower symbol) and 0.5η (upper symbol) at constant α/β.

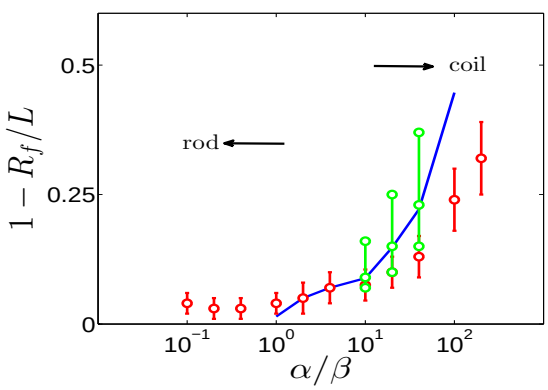

Fig. 11 Effictive compresion $1 - R_f/L$ as a function of α/β determined from the planar motion of the Langevin filament (solid blue line) and the 2D motion of the DPD bead-spring chain (open red symbols) with $\alpha = 10.0$. The green symbols represent the variation of R_f/L as the hydrodynamic resistance coefficients in the continuum model are changed from η to 2η (upper symbol) and 0.5η (lower symbol) at constant α/β.

be

$$\tau_R \propto \frac{\eta\left(\left(\frac{L}{l_P}\right)^{\nu} l_P\right)^3}{k_B T} \propto \frac{\eta L^3 \beta^{3(1-\nu)}}{k_B T} \tag{22}$$

where ν is the Flory index and we take $\nu = 0.5$ for theta solvent in our simulation. Thus, we end up with another Weissenberg number $W = \alpha\beta^{3/2}$ and its limiting value indicate for: ($W \to \infty$) a nearly-rigid rod dominated by bending elasticity with negligible thermal fluctuations, while for ($W \to 0$) a flexible string dominated by Brownian forces. However, W is only suitable for fiber under positive tension (extension relaxation). The effects of W on fiber dynamics under negative tension are difficult to understand, hence, a new dimensionless number is required to capture accurately the physics of fiber dynamics under negative tension and thermal fluctuations.

5 Summary and Discussion

We considered here the dynamic response of a single inextensible, elastic filament subject to stretching/compression in a stagnation-point flow. We developed two different models, the first based on a stochastic PDE treating the filament as continuum, and the second based on dissipative particle dynamics (DPD) treating the filament as bead-spring chain. In the second model, the two-dimensional stagnation-point flow is achieved by driving the particles with a body force derived from the pressure gradient of a potential flow in a lattice of vortices. In both models, the elastic properties are matched and the filament motion is constrained to the plane. In the DPD simulations the solvent is simulated explicitly and the corresponding particles are free to move in three-dimensions. On the other hand, in the continuum model, the solvent is simulated implicitly with the friction acting on the filament derived from the Stokes equation for a rigid rod subject to three-dimensional flow. The latter is subject to uncertainties, which we investigate by varying the magnitude of the friction coefficient by $\pm 50\%$. In particular, we were interested in investigating the effect of thermal fluctuations on the dynamic response of the filament and the presence of a possible stretch-coil instability from two different modeling perspectives. We found that the filament displays a buckling instability induced by tension, analogous to the Euler beam, at Weissenberg number of order one. Above this value, both the temporal and spatial thermal noise are amplified due to interaction between the thermal fluctuations and the nonlinear filament dynamics. Normal mode analysis of the filament motion obtained by both models shows the response to be composed of the same modes, but the transition from nearly straight rods to loose coils suggests that constant resistance coefficients may overestimates the amplitude of the filament response. Although we have dealt only with the single continuous filament dynamics in an undisturbed stretching flow, the framework employed and numerical schemes can be applied to concentrated filament solutions and filament networks with large disturbances of the flow field, where a Stokes or a Navier-Stokes solver should be employed together with our current frameworks [47]. Comparing with previous studies [2], we considered the stochastic Brownian force in the governing equation of fiber dynamics. Without thermal fluctuations (or temperature), the fiber only exhibits a single mode subjected to specific tension. However, a configuration is a summation of each normal mode with different modal energy in the finite temperature case, where the modal energy follows or deviates from the equi-partition theorem before and after the bifurcation point, respectively. Indeed, the bifurcation point ($\alpha/\beta \sim \mathcal{O}(1)$) is independent of the temperature, but the fiber dynamics is highly dependent on the tem-

perature. Before the bifurcation point, the dynamics depends linearly on temperature since the modal energies can be well separated and scaled by thermal energy. However, the nonlinear dependence of fiber dynamics on thermal fluctuations is extremely complicated after the bifurcation point and deserves further studies.

6 Acknowledgments

This work was sponsored by the Collaboratory on Mathematics for Mesoscopic Modeling of Materials (CM4) supported by DOE, and also by NIH grant (1U01HL114476-01A1). Computations were performed using a DOE INCITE award. We would like to acknowledge Dr. Zhongqiang Zhang of Worcester Polytechnic Institute (WPI) for helpful discussions.

References

1 L. Guglielmini, A. Kushwaha, E. Shaqfeh and H. Stone, *Phys. Fluids*, 2012, **24**, 123601.

2 F. Thuroff, B. Obermayer and E. Frey, *Phys. Rev. E*, 2011, **83**, 021802.

3 Y. Bohbot-Raviv, W. Zhao, M. Feingold, C. Wiggins and R. Granek, *Phys. Rev. Lett.*, 2004, **92**, 098101.

4 B. Obermayer, O. Hallatschek, E. Frey and K. Kroy, *Eur. Phys. J. E*, 2007, **23**, 375.

5 O. Hallatschek, E. Frey and K. Kroy, *Phys. Rev. E*, 2007, **75**, 031905.

6 Y. Juang, S. Wang, X. Hu and L. Lee, *Phys. Rev. Lett.*, 2004, **93**, 268105.

7 C. Cyron and W. A. Wall, *Phys. Rev. E*, 2009, **80**, 066704.

8 C. Cyron and W. A. Wall, *Int. J. Numer. Meth. Eng.*, 2012, **90**, 955.

9 S. Olson, S. Lim and R. Cortez, *J. Comp. Phys.*, 2013, **238**, 169.

10 E. Hinch, *J. Fluid Mech.*, 1976, **75**, 765.

11 R. M. Jendrejack, J. J. de Pablo and M. D. Graham, *J.Chem. Phys.*, 2002, **116**, 7755.

12 T. Munk, O. Hallatschek, C. Wiggins and E. Frey, *Phys. Rev. E*, 2006, **74**, 041911.

13 P. S. Doyle, E. S. G. Shaqfeh and A. P. Gast, *J. Fluid Mech.*, 1997, **334**, 251.

14 V. Symeonidis, G. Karniadakis and B. Caswell, *Phys Rev. Lett.*, 2006, **124**, 184101.

15 M. Harasim, B. Wunderlich, O. Peleg, M. Kroger and A. Bausch, *Phys. Rev. Lett.*, 2013, **110**, 108302.

16 V. Kantsler and R. E. Goldstein, *Phys. Rev. Lett.*, 2012, **108**, 038103.

17 Y. Young and M. Shelley, *Phys. Rev. Lett.*, 2007, **99**, 058303.

18 A. Evans, S. Spagnolie, D. Bartolo and E. Lauga, *Soft Matter*, 2013, **9**, 1711.

19 L. Li, H. Manikantan, D. Saintillan and S. Spagnolie, *J. Fluid Mech.*, 2013, **735**, 705.

20 L. Blanchoin, R. Boujemaa-Paterski, C. Sykes and J. Plastino, *Physiol Rev.*, 2014, **94**, 235.

21 E. Hinch, *J. Fluid Mech.*, 1994, **271**, 219.

22 S. Panyukov and Y. Rabin, *Phys. Rev. Lett.*, 2000, **85**, 2404.

23 V. Kantsler and E. Segre, *Phys. Rev. Lett.*, 2007, **99**, 178102.

24 M. Levant and V. Steinberg, *Phys. Rev. Lett.*, 2012, **109**, 268103.

25 A. Montesi, D. Morse and M. Pasquali, *J. Chem. Phys.*, 2005, **122**, 084903.

26 J. Deschamps, V. Kantsler, E. Segre and V. Steinberg, *Proc. Natl. Acad. Sci. USA*, 2009, **106**, 11444.

27 K. Turitsyn and S. Vergeles, *Phys. Rev. Lett.*, 2008, **100**, 028103.

28 M. Doi and S. Edwards, *The Theory of Polymer Dynamics*, Oxford Unverisity Press, Oxford, 1986.

29 R. Goldstein and S. A. Langer, *Phys. Rev. Lett.*, 1995, **75**, 1094.

30 K. Nakayama, H. Segur and M. Wadati, *Phys. Rev. Lett.*, 1992, **69**, 2603.

31 F. Gittes, B. Mickey, J. Nettleton and J. Howard, *J. Cell Biology*, 1993, **120**, 923.

32 T. Squires and J. Brady, *Phys. Fluids*, 2005, **17**, 073101.

33 H. Manikantan and D. Saintillan, *Phys. Fluids*, 2013, **25**, 073603.

34 R. Lagnado and L. Leal, *Experiments in Fluids*, 1990, **9**, 25.

35 H. Yang, C. Park, Y. Hu and L. Leal, *Phys. Fluids*, 2001, **13**, 1087.

36 K. Roth, C. Eggleton, K. Neeves and D. Marr, *Lab Chip*, 2013, **13**, 1571.

37 D. Pan, N. Phan-Thien, N. Mai-Duya and B. C. Khoo, *J.Comp. Phys.*, 2013, **242**, 196.

38 A. Chorin, *J. Comp.. Phys.*, 1997, **135**, 118.

39 C. Gear, *Numerical Initial Value problems in Ordinary Dierential Equations*, Prentice Hall PTR, Upper Saddle River, NJ, USA, 1971.

40 P. Hoogerbrugge and J. Koelman, *Europhys. Lett.*, 1992, **19**, 155.

41 R. Groot and P. Warren, *J. Chem. Phys.*, 1997, **107**, 4423.

42 M. Deng, X. Li, H. Liang, B. Caswell and G. Karniadakis, *J. Fluid Mech.*, 2012, **711**, 192.

43 P. Espanol and P. Warren, *Europhys. Lett.*, 1995, **30**, 191.

44 S. Plimpton, *J. Comp. Phys.*, 1995, **117**, 1.

45 C. Wiggins, D. Riveline, A. Ott and R. Goldstein, *Biophys. J.*, 1998, **74**, 1043.

46 B. H. Zimm, *J. Chem. Phys.*, 1956, **24**, 269.

47 J. Chrispell, L. Fauci and M. Shelley, *Phys. Fluids*, 2013, **25**, 013103.

7 Appendix: Proper Orthogonal Decomposition Analysis

Proper Orthogonal Decomposition (POD) is a spectral analysis tool often employed for data compression and low-dimensional modeling, which is also known as principal component analysis (PCA), singular value decomposition (SVD). Here, POD decomposes the time-space fiber configuration $\theta(t,s)$ into an expansion of orthogonal temporal and spatial modes, i.e.,

$$\theta(t,s) = \sum_{q=1}^{N_{pod}} \phi_q(s) a_q(t) \tag{23}$$

To compute the space- time- POD modes, a temporal auto-correlation covariance matrix **C** is constructed from the inner product of $\theta(\tau^i,s)$ and $\theta(\tau^j,s)$ as

$$C_{ij} = \int \theta(\tau^i,s)\theta(\tau^j,s)ds, \qquad ,i,j = 1,2,...,N_{POD} \tag{24}$$

The temporal modes $a_q(t)$ are the eigenvectors of **C**, and the spatial modes $\phi_q(s)$ are computed via orthogonality relations, i.e.,

$$\phi_q(s) = \int a_q(t)\theta(\tau,s)d\tau \tag{25}$$

In a time average sense, the real dynamic modes can be obtained numerically via Proper Orthogonal Decomposition over a certain time window. For example, we chose the time window to be before significant buckling and reorientation, and obtain the POD modes. They correspond to the analytical eigen-modes obtained by Kantsler et al.[16], as can be seen in Figure (12).

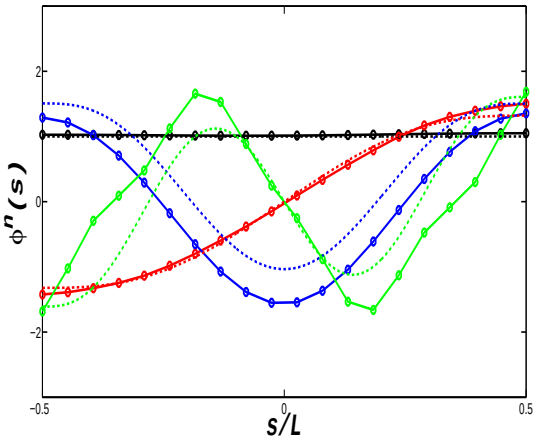

Fig. 12 First four eigen-modes for the full biharmonic operator with natural boundary conditions; the dash lines are the analytical resutls obtained by Kantsler et al.[16] with known tension, and the symbols represent the eigen-modes obtained with POD within a short time period for fiber aligned along the stretching axis.

The eigenvalues λ_k of the autocorrelation matrix **C** (with $\lambda_1 > \lambda_2 > ... > \lambda_{N_{pod}}$) represent the energy level associated with the POD mode q, as shown in Figure (13)

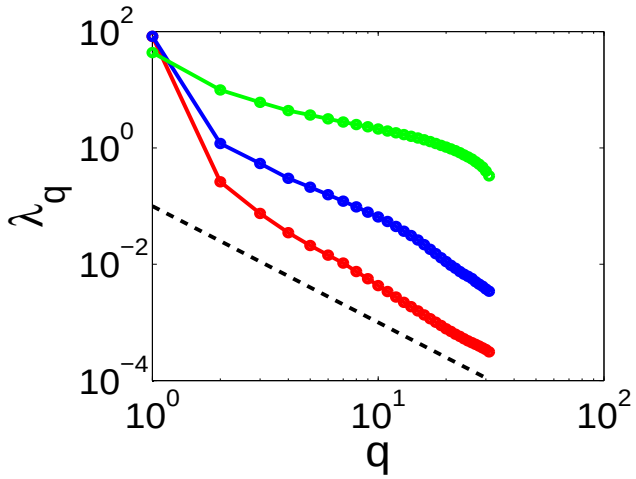

Fig. 13 POD modes energy as functions of mode number q, with $\alpha/\beta = 100.0$ (red), 10.0 (blue), 1.0 (green).

As expected, we observe a typical power-law decay of high-order POD modes in all simulations. For $\alpha/\beta \leq 1$, the power-law decay corresponds to a thermal white-noise energy spectrum indicated by black dashed line (slope = 2.0) in the plots,

and only small amount of POD modes are enough to characterize the fiber dynamics. However, the power-law decay becomes slower as we increase α/β, which shows that the fiber dynamics is accompanied by the excitement of high-order deformation modes, and hence more degrees of freedoms are needed to describe such motions. In general, POD and normal modes analysis reveal the same physics as described above.